catalysts

MDPI

Article

# Dolomite-Derived Ni-Based Catalysts with Fe Modification for Hydrogen Production via Auto-Thermal Reforming of Acetic Acid

**Xinyan Zhong [1], Wei Xie [1], Ning Wang [2], Yiping Duan [1], Ruishu Shang [1] and Lihong Huang [1,3,*]**

[1] Department of Chemical and Pharmaceutical Engineering, Chengdu University of Technology, Chengdu 610059, China; xinyan_zhong@yahoo.com (X.Z.); xiewei0403@yahoo.com (W.X.); duanyipingyznu@yahoo.com (Y.D.); shangruishu@yahoo.com (R.S.)

[2] Department of Chemical Engineering, Tsinghua University, Beijing 100084, China; maibucongtouyue@163.com

[3] Richard G. Lugar Center for Renewable Energy, Indiana University-Purdue University, Indianapolis, IN 46224, USA

* Correspondence: huanglihong06@cdut.cn or lihhuang@iupui.edu; Tel.: +86-28-8407-8939; Fax: +86-28-8407-9074

Academic Editor: Ivan V. Kozhevnikov

Received: 18 May 2016; Accepted: 8 June 2016; Published: 15 June 2016

**Abstract:** Bio-oil can be obtained via fast pyrolysis of biomass, and typically contains acetic acid (~30 mass %). The acetic acid has often been tested as a model compound for hydrogen production via reforming bio-oil, in which catalysts are a key factor for stable hydrogen production. However, deactivation of catalysts by coking and oxidation hinders the application of the reforming process. Dolomite-derived Ni-based catalysts with Fe additive, $MgNi_{0.2}Ca_{0.8-x}Fe_xO_{2\pm\delta}$ ($x$ = 0–0.8), were successfully synthesized by the hydrothermal synthesis method, and then tested in auto-thermal reforming (ATR) of acetic acid (AC). The $MgNi_{0.2}Ca_{0.5}Fe_{0.3}O_{2\pm\delta}$ catalyst performed a stable reactivity in ATR: the conversion of AC reached 100%, and the $H_2$ yield remained stable around 2.6 mol-$H_2$/mol-AC. The catalysts were characterized by X-ray diffraction (XRD), $N_2$ physisorption, X-ray photoelectron spectra (XPS), $H_2$-temperature-programmed reduction (TPR), inductively coupled plasma- atomic emission spectroscopy (ICP-AES) and Thermogravimetry (TG); the results show that a periclase-like solid solution of Mg(Ni,Fe)O and lime were formed via the precursors of dolomite and hydrotalcite, and then transformed into Fe-rich Ni-Fe alloy with basic support of MgO-CaO after reduction. The stable $Ni^0$ spices with basic support can explain the stability and resistance to coking during ATR of AC.

**Keywords:** dolomite-derived Ni-based catalyst; auto-thermal reforming of acetic acid; hydrothermal synthesis; Ni-Fe alloy; bio-oil

## 1. Introduction

Hydrogen has long been viewed as a clean energy carrier, and can be extracted via reforming of fossil resources, e.g., natural gas or coal. Biomass is an important alternative renewable $CO_2$-neutral resource for hydrogen production, while bio-oil produced via fast-pyrolysis of biomass is attracting attention for its high energy density and transportation convenience [1–3]. Within bio-oil, acetic acid (AC) is one of the major components (~30 mass %), and has often been tested as a model compound for hydrogen production via processes of steam reforming (SR, $CH_3COOH + 2H_2O \rightarrow 2CO_2 + 4H_2 - 131.4$ kJ/mol) [2,4,5].

SR is a strong endothermic process and requires an external heat sources [1,6], while auto-thermal reforming (ATR) with endothermic steaming reforming (SR) and exothermic partial oxidation reaction

(POX) can be a solution for heat balance via adjusting the feed proportions of oxygen, acetic acid (AC), and steam, e.g., $CH_3COOH + 1.44H_2O+0.28O_2 \rightarrow 2CO_2 + 3.44H_2$ [1,7].

However, coke deposition can be a concern. For example, Ni-based catalysts have been widely investigated due to its high catalytic activity for breakage of C–C in the reforming process; on the other hand, acidic sites within the supports of $Al_2O_3$ or $ZrO_2$ favor decomposition and polymerization of AC with derivatives of acetone, ethylene, *etc.*, resulting in carbon deposition [4,8]. Therefore, oxides of alkaline earth metals with basic sites, e.g., MgO and CaO, have been used as supports or additives and proved effective to suppress coking over acidic sites [9–11].

There are other issues within ATR as well: because of the oxidative atmosphere and high temperature (up to 1000 °C) in the upstream zone of the fixed-bed reactor for ATR, oxidation and sintering of metallic Ni occurred and resulted in catalyst deactivation [1,12].

Dolomite, or calcium magnesium carbonate with well-dispersed species of calcium, magnesium, and nickel, can be a promising candidate for ATR of AC. Within dolomite-derived Ni-based catalysts, alkaline earth oxides of CaO and MgO with Lewis basic sites could promote adsorption and migration of $H_2O$ and OH groups over the catalyst's surface, and promote carbon gasification and reduce carbon deposition [9,10,13]. Meanwhile, Ca or Mg can be partly replaced by active component of Ni in a form of solid solution, e.g., Ni inserted in the skeleton of periclase as Mg(Ni)O to improve dispersion and thermal stability [12]. For the issue of Ni oxidation, additive of Fe was proved effective to resist oxidation of Ni species [12,14]. Regarding the preparation method of catalysts, a synthesis strategy, e.g., hydrothermal synthesis, has long been used to synthesize catalysts with high porosity and dispersion of active components [15,16].

In the present work, precursors with a dolomite structure were fabricated via hydrothermal synthesis, and calcium was partly replaced by an active component of nickel and an additive of iron. These dolomite-derived catalysts ($MgNi_{0.2}Ca_{0.8-x}Fe_xO_{2\pm\delta}$ ($x$ = 0–0.8)) were then tested in ATR of AC for hydrogen production, and characterizations of X-ray diffraction (XRD), X-ray photoelectron spectra (XPS), TPR, *etc.* were conducted to study the relationship between structure and reactivity. To the best of the authors' knowledge, these dolomite-derived $MgNi_{0.2}Ca_{0.8-x}Fe_xO_{2\pm\delta}$ catalysts have not been reported for ATR of AC for hydrogen production, and are listed in Table 1.

**Table 1.** The list of Ni-based dolomite-derived catalysts with Fe promotion as prepared.

| Catalysts | Nominal Molar Composition | Weight Compositions Analyzed by ICP-AES/% | | | | Surface Area/($m^2$/g) | Average Pore Size/nm |
|---|---|---|---|---|---|---|---|
| | | MgO | NiO | CaO | $Fe_2O_3$ | | |
| $MNC_{0.8}F_{0.0}$ | $MgNi_{0.2}Ca_{0.8}O_{2\pm\delta}$ | 39.12 | 15.11 | 45.77 | 0.00 | 4.27 | 7.44 |
| $MNC_{0.7}F_{0.1}$ | $MgNi_{0.2}Ca_{0.7}Fe_{0.1}O_{2\pm\delta}$ | 38.42 | 14.40 | 39.67 | 7.51 | 6.62 | 6.52 |
| $MNC_{0.5}F_{0.3}$ | $MgNi_{0.2}Ca_{0.5}Fe_{0.3}O_{2\pm\delta}$ | 37.74 | 13.91 | 26.33 | 22.02 | 8.71 | 6.16 |
| $MNC_{0.3}F_{0.5}$ | $MgNi_{0.2}Ca_{0.3}Fe_{0.5}O_{2\pm\delta}$ | 34.84 | 13.29 | 16.68 | 35.19 | 11.53 | 5.87 |
| $MNC_{0.0}F_{0.8}$ | $MgNi_{0.2}Fe_{0.8}O_{2\pm\delta}$ | 33.01 | 12.31 | 0.00 | 54.68 | 4.69 | 5.37 |

## 2. Results

### *2.1. Auto-Thermal Reforming of Acetic Acid*

ATR of acetic acid (AC), $CH_3COOH + 1.44H_2O + 0.28O_2 \rightarrow 2CO_2 + 3.44H_2$, was conducted over the Ni-based dolomite-derived catalysts at conditions of 650 °C, 3.6 g-AC/(g-catalyst.h) and 1 atm for 10 h. For the iron-free catalyst of $MNC_{0.8}F_{0.0}$ (Figure 1a), the AC conversion started near 99.0% and decreased slightly to 97.2% in the end, while the $H_2$ yield was recorded near 2.1 mol-$H_2$/mol-AC. 1 mol-$H_2$/mol-AC, as indicated in Table 2 of the average activity data during the ATR process. For the carbon-containing products, the selectivity to $CO_2$ and CO remained stable near 67.1% and 18.7%, respectively, and the selectivity to $CH_4$ was recorded near 3.3%. In the meantime, the selectivity to acetone varied near 10.4%, suggesting that part of acetic acid was transformed into acetone via the ketonization route ($2CH_3COOH \rightarrow CH_3COCH_3 + CO_2 + H_2O$) and the produced acetone has not been converted via reaction of steam reforming ($CH_3COCH_3 + 5H_2O \rightarrow 3CO_2 + 8H_2$) [17,18].

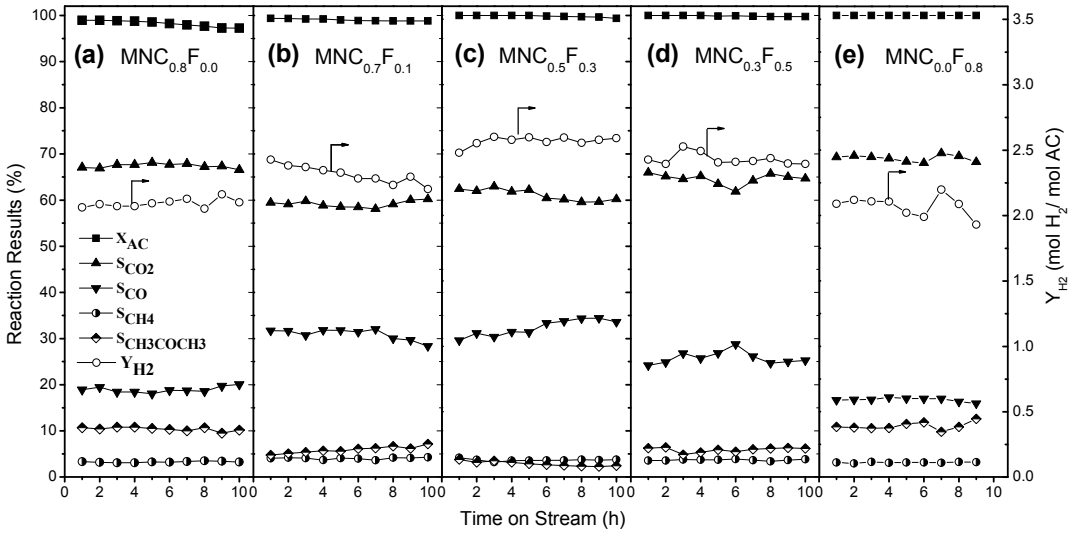


**Figure 1.** Auto-thermal reforming (ATR) of acetic acid (AC) over Ni-based catalysts at 650 °C, 3.6 g-AC/(g-catalyst.h) and 1 atm. (**a**) $MNC_{0.8}F_{0.0}$; (**b**) $MNC_{0.7}O_{0.1}$; (**c**) $MNC_{0.5}F_{0.3}$; (**d**) $MNC_{0.3}F_{0.5}$; (**e**) $MNC_{0.0}F_{0.8}$.

**Table 2.** The average data of ATR of acetic acid over Ni-based catalysts at 650 °C, 3.6 g-AC/(g-catalyst.h) and 1 atm.

| Catalysts | $X_{AC}$ | $S_{CO}$ | $S_{CO_2}$ | $S_{CH_4}$ | $S_{CH_3COCH_3}$ | $Y_{H_2}$ |
|---|---|---|---|---|---|---|
| $MNC_{0.8}F_{0.0}$ | 98.2 | 67.4 | 18.9 | 3.3 | 10.4 | 2.09 |
| $MNC_{0.7}F_{0.1}$ | 99.0 | 59.1 | 30.9 | 4.0 | 5.9 | 2.31 |
| $MNC_{0.5}F_{0.3}$ | 99.9 | 61.1 | 32.3 | 3.7 | 2.9 | 2.59 |
| $MNC_{0.3}F_{0.5}$ | 99.9 | 64.6 | 25.8 | 3.7 | 5.9 | 2.43 |
| $MNC_{0.0}F_{0.8}$ | 100.0 | 69.1 | 16.7 | 3.2 | 11.0 | 2.07 |

With calcium partially replaced by iron in $MNC_{0.7}F_{0.1}$ (Figure 1b), the conversion of AC reached 99.3% in the beginning and remained stable, while the $H_2$ yield was improved and varied within 2.21–2.43 mol-$H_2$/mol-AC. The improvement of $H_2$ yield can be attributed to decrease of the selectivity to acetone near 5.90%, suggesting that the ketonization route was constrained. Meanwhile, the selectivity to $CO_2$ and CO remained near 59.2% and 30.9%, respectively.

For $MNC_{0.5}F_{0.3}$ in Figure 1c, a better performance of activity and stability was observed: the AC disappeared in the product gas, and the $H_2$ yield reached 2.6 mol-$H_2$/mol-AC and remained stable during the 10-h ATR test. In the meantime, the selectivity to acetone decreased to 2.9% over time; on the other hand, the selectivity to $CO_2$ and CO varied near 61.1% and 32.3%, respectively; the selectivity to $CH_4$ remained stable around 3.7%. The reactivity of $MNC_{0.5}F_{0.3}$ was similar to an olivine-derived catalyst of $Mg_{1.7}Ni_{0.3}SiO_4$, which was tested at a much higher temperature of 800 °C and hydrogen yield was recorded near 2.73–3.06 mol-$H_2$/mol-AC [7]. Another Ni-Co bi-metal catalyst of ($Ni_{0.2}Co_{0.8}Mg_6O_{7\pm\delta}$) was tested in endothermic process of steam reforming (SR) of AC, instead of ATR, and a hydrogen yield of 2.6–3.1 mol-$H_2$/mol-AC was obtained at 600 °C [19].

With the increasing iron in $MNC_{0.3}F_{0.5}$ (Figure 1d), the $H_2$ yield dropped slightly to about 2.4 mol-$H_2$/mol-AC, and the conversion of AC reached 100%, while the selectivity to acetone increased slightly to 5.9%.

Over the Ca-free catalyst of $MNC_{0.0}F_{0.8}$ (Figure 1e), the $H_2$ yield decreased to 2.1 mol-$H_2$/mol-AC. This lower $H_2$ yield can be attributed to a higher selectivity to acetone, which reached 12.6% in the end.

The $MNC_{0.5}F_{0.3}$ catalyst produced a stable $H_2$ yield at 650 °C, and was further tested from 500 °C to 800 °C to analyze the effect of temperatures. As shown in Figure 2a, over the $MNC_{0.5}F_{0.3}$ catalyst, the conversion of AC started near 97.9% at 500 °C, and reached 100% as the temperature increased

to 550 °C or higher. In the meantime, the $H_2$ yield was obtained at 1.38 mol-$H_2$/mol-AC at 500 °C, and this low yield can be attributed to high selectivity to the byproduct of acetone near 15.06%. With increasing temperatures, the selectivity to acetone decreased continuously and disappeared at 700 °C. As a result, the $H_2$ yield increased and reached 2.89 mol-$H_2$/mol-AC. With higher temperatures up to 800 °C, the $H_2$ yield dropped to about 2.65 mol-$H_2$/mol-AC because the selectivity to methane increased to 10.85% via thermal decomposition of acetic acid ($CH_3COOH \rightarrow CH_4 + CO_2$).

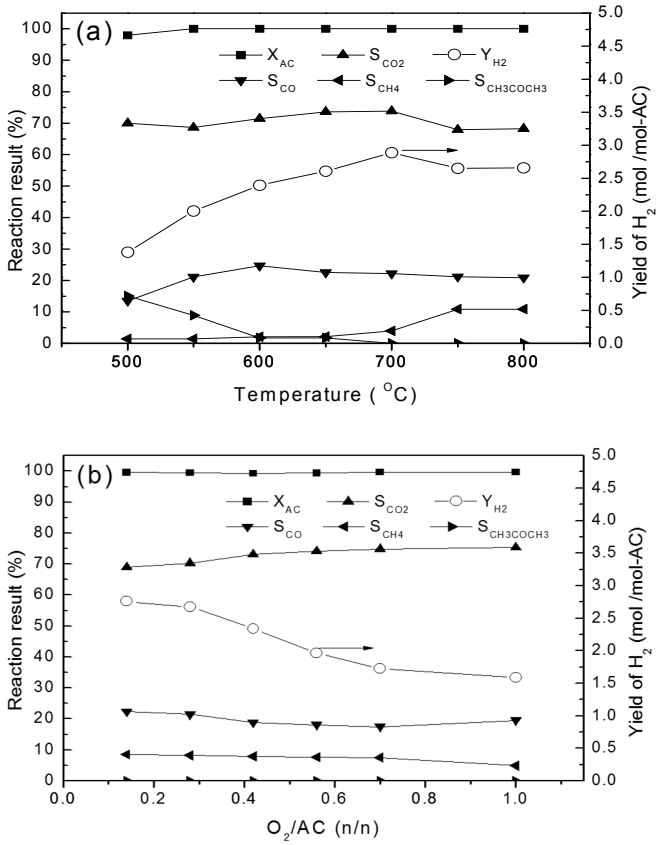


**Figure 2.** (**a**) Effect of temperature on the catalytic performance of $MNC_{0.5}F_{0.3}$ in ATR of AC at 3.6 g-AC/(g-catalyst.h) and 1 atm; (**b**) effect of $O_2$/AC on the catalytic performance of $MNC_{0.5}F_{0.3}$ in ATR at 3.6 g-AC/(g-catalyst.h), 1 atm and 650 °C.

The effect of $O_2$/AC in feed was tested as well. As shown in Figure 2b, with different ratio of $O_2$/AC up to 1.0, the conversion of AC remained stable near 100%, while the $H_2$ yield was recorded near 2.79 mol-$H_2$/mol-AC at $O_2$/AC = 0.14; with higher $O_2$/AC, the $H_2$ yield dropped slightly to 2.67 mol-$H_2$/mol-AC at $O_2$/AC = 0.28 and further to 1.59 mol-$H_2$/mol-AC when $O_2$/AC reached 1.0. Meanwhile, the selectivity to $CO_2$ increased with higher ratio of $O_2$/AC. The selectivity to $CH_4$ decreased, suggesting that $O_2$ in ATR of AC was helpful to convert $CH_4$. Considering the heat balance in ATR, the ratio of $O_2$/AC near 0.28 can be adopted with heat balance and high catalytic performance.

## *2.2. Characterizations*

### 2.2.1. Precursors of Catalysts

To find the structure variation of these Ni-based catalysts with Ca replaced by Fe, the precursors were firstly characterized by X-ray diffraction (XRD). For the iron-free catalyst of $MNC_{0.8}F_{0.0}$ ($MgNi_{0.2}Ca_{0.8}O_{2\pm\delta}$) in Figure 3a(1), strong peaks at 30.9°, 37.4°, 41.1°, 50.5°, and 51.0° indicate that a main structure of dolomite ($CaMg(CO_3)_2$, JCPDS: 36-0426) was successfully synthesized. Meanwhile,

the brucite structure ($Mg(OH)_2$, JCPDS: 86-0441) with a similar structure of $Ni(OH)_2$ (JCPDS: 14-0117) were observed, and traces of calcite ($CaCO_3$, JCPDS: 05-0586) can be found as well.

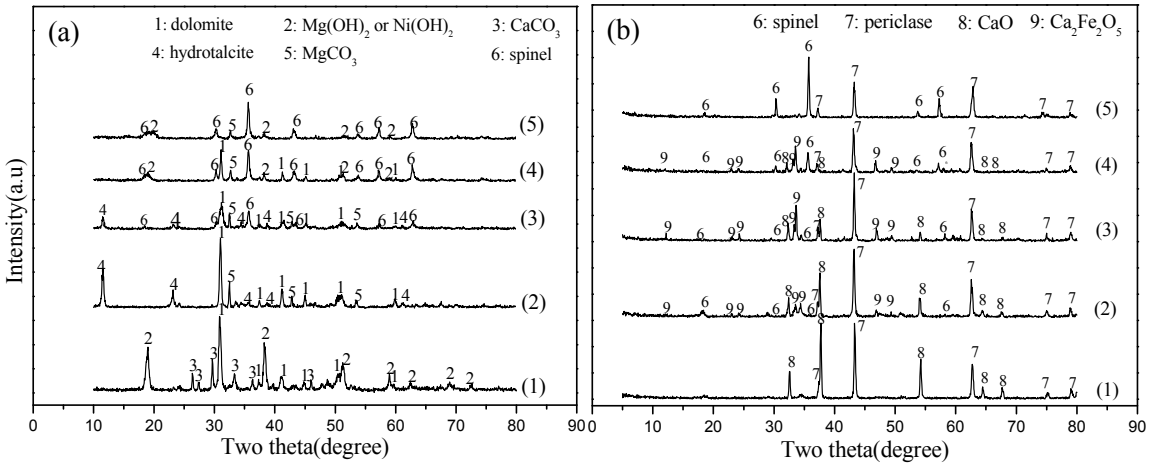


**Figure 3.** X-ray diffraction (XRD) patterns of Ni-based catalysts of (**a**) precursors and (**b**) oxides after calcination at 800 °C. (1) $MNC_{0.8}F_{0.0}$; (2) $MNC_{0.7}F_{0.1}$; (3) $MNC_{0.5}F_{0.3}$; (4) $MNC_{0.3}F_{0.5}$; and (5) $MNC_{0.0}F_{0.8}$.

With Ca partly replaced by Fe in $MNC_{0.7}F_{0.1}$ ($MgNi_{0.2}Ca_{0.7}Fe_{0.1}O_{2\pm\delta}$), as shown in Figure 3a(2), the dolomite structure still remained as the main crystal phase, but calcite disappeared; meanwhile, there were peaks of hydrotalcite ($Ni_{0.75}Fe_{0.25}(CO_3)_{0.125}(OH)_2.(H_2O)_{0.38}$, JCPDS: 40-0215) and traces of magnesite ($MgCO_3$, JCPDS:08-0479).

With decreasing calcium and increasing iron in $MNC_{0.5}F_{0.3}$ and $MNC_{0.3}F_{0.5}$ (Figure 3a(3,4)), peaks of dolomite and hydrotalcite became weaker. Meanwhile, similar iron-containing spinel phases ($MgFe_2O_4$ (JCPDS: 73-2211), $Fe_3O_4$ (JCPDS: 75-0449), or $NiFe_2O_4$ (JCPDS: 74-2081)) [20] were observed and became stronger.

For the calcium-free catalyst of $MNC_{0.0}F_{0.8}$ ($MgNi_{0.2}Fe_{0.8}O_{2\pm\delta}$) in Figure 3a(5), iron-containing spinel phases became the main crystal phases, while calcium-containing phases of dolomite, calcite and hydrotalcite disappeared.

### 2.2.2. Oxides of Catalysts

The precursors were then calcined at 800 °C and scanned by XRD, as depicted in Figure 3b. For $MNC_{0.8}F_{0.0}$ without iron (Figure 3b(1)), after calcination, the main phases of dolomite, brucite, and calcite were decomposed and transformed into lime (CaO, JCPDS: 74-1226) and periclase (MgO, JCPDS: 65-0476). For the nickel species, because of the similar crystal structure of NiO and MgO, the nickel species probably existed in the solid solution as Mg(Ni)O, for example, $Mg_{0.6}Ni_{0.4}O$ (JCPDS: 65-2901) or $MgNiO_2$ (JCPDS: 24-0712) [12,14].

With calcium partly replaced by iron in $MNC_{0.7}F_{0.1}$ (Figure 3b(2)), in addition to the main phases of periclase and CaO, traces of iron-containing spinel phase ($MgFe_2O_4$, $Fe_3O_4$ or $NiFe_2O_4$) and brownmillerite-type species ($Ca_2Fe_2O_5$, JCPDS:71-2264) were found.

With more iron species in $MNC_{0.5}F_{0.3}$ and $MNC_{0.3}F_{0.5}$, the periclase phase of Mg(Ni)O was still the main phase, and peaks of CaO became weaker and almost disappeared. In contrast, iron-containing spinel phases became stronger, while $Ca_2Fe_2O_5$ can still be tracked.

For the Ca-free catalyst of $MNC_{0.0}F_{0.8}$, there were only two main phases of periclase and spinel ($MgFe_2O_4$, $Fe_3O_4$, or $NiFe_2O_4$).

In order to understand texture properties in these catalysts, $N_2$ physisorption was carried out, and the surface area ($S_{BET}$) and pore distribution were analyzed, as shown in Table 1. The $S_{BET}$ of the Fe-free catalyst of $MNC_{0.8}F_{0.0}$ was recorded at 4.27 $m^2/g$; with Ca gradually replaced by Fe, the $S_{BET}$

increased and reached 11.53 $m^2/g$ over $MNC_{0.3}F_{0.5}$, suggesting that iron could be inserted into the periclase structures as Mg(Ni, Fe)O, resulting in higher surface area [14]. For the Ca-free catalyst of $MNC_{0.0}F_{0.8}$, $S_{BET}$ dropped to 4.7$m^2/g$, which can be attributed to the dominant phase of spinel with low surface area, as shown in Figure 3b.

### 2.2.3. Reduced Catalysts

To find the state of active components before reaction, the catalysts were reduced at 650 °C for 1 h and then scanned by XRD, as shown in Figure 4a. For the iron-free catalyst of $MNC_{0.8}F_{0.0}$, the two main phases of periclase and lime still remained, and no $Ni^0$ species were detected, suggesting that the Ni species in periclase-like phase of Mg(Ni)O may either have not been reduced, or have been reduced into amorphous $Ni^0$, and cannot be detected by XRD, which needs to be further checked by XPS later.

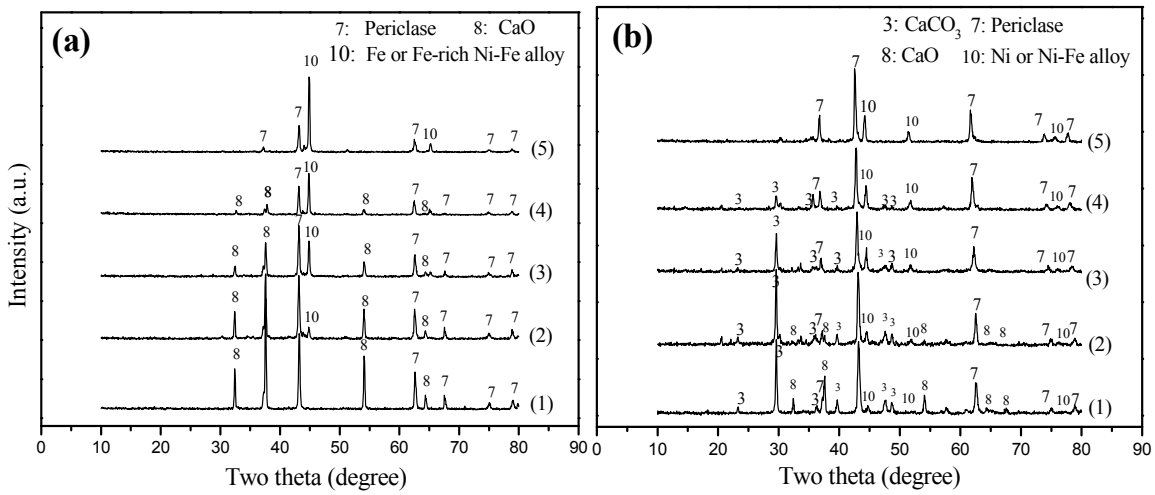


**Figure 4.** XRD patterns of Ni-based catalysts of (**a**) reduced at 650 °C and (**b**) spent after ATR. (1) $MNC_{0.8}F_{0.0}$; (2) $MNC_{0.7}F_{0.1}$; (3) $MNC_{0.5}F_{0.3}$; (4) $MNC_{0.3}F_{0.5}$; and (5) $MNC_{0.0}F_{0.8}$.

With Ca gradually replaced by Fe in $MNC_{0.7}F_{0.1}$, $MNC_{0.5}F_{0.3}$, $MNC_{0.3}Fe_{0.5}$, and $MNC_{0.0}F_{0.8}$, as shown in (Figure 4a), the iron-containing species of $Ca_2Fe_2O_5$ and spinel phases ($MgFe_2O_4$, $Fe_3O_4$ or $NiFe_2O_4$) disappeared after reduction at 650 °C. Accordingly, peaks of metallic α-Fe (JCPDS: 03-1050) or similar Fe-rich Ni-Fe alloy (JCPDS: 03-1049) were observed and became stronger. Meanwhile, the peaks of periclase gradually shrank, suggesting that more Ni species and Fe species could also be reduced from the mixed solid solution of Mg(Ni, Fe)O.

For the Ca-free catalyst of $MNC_{0.0}F_{0.8}$, the lime phase disappeared, and the periclase phase remained weaker, while the peaks of Fe or Ni-Fe alloy became the main phase.

XRD cannot identify $Ni^0$ and $Fe^0$ species in the amorphous state; however, XPS are more sensitive to the electronic state of Ni and Fe species. Therefore, XPS was conducted over the reduced catalysts of $MNC_{0.8}F_{0.0}$, $MNC_{0.5}F_{0.3}$ and $MNC_{0.0}F_{0.8}$. As shown in Figure 5a–c of Ni $2p_{3/2}$, there are peaks near binding energies at 852.1 eV and 854.0 eV, which can be attributed to the characteristic peaks of $Ni^0$ and $Ni^{2+}$, respectively, while the peak near 861.0 eV can be assigned to shake-up peak of $Ni^{2+}$ species [21]. The semi-quantitative analysis was conducted via the peak areas: over these reduced catalysts, the molar ratio of $Ni^0/(Ni^0 + Ni^{2+})$ was recorded near 9.0% in $MNC_{0.8}F_{0.0}$, 12.5% in $MNC_{0.5}F_{0.3}$, and 14.1% in $MNC_{0.0}F_{0.8}$, respectively, as shown in Table 3. The results indicate that the addition of Fe can promote to reduction of Ni species from the periclase phase of Mg(Ni,Fe)O, and is consistent with the shrank peaks of periclase in XRD (Figure 4a).

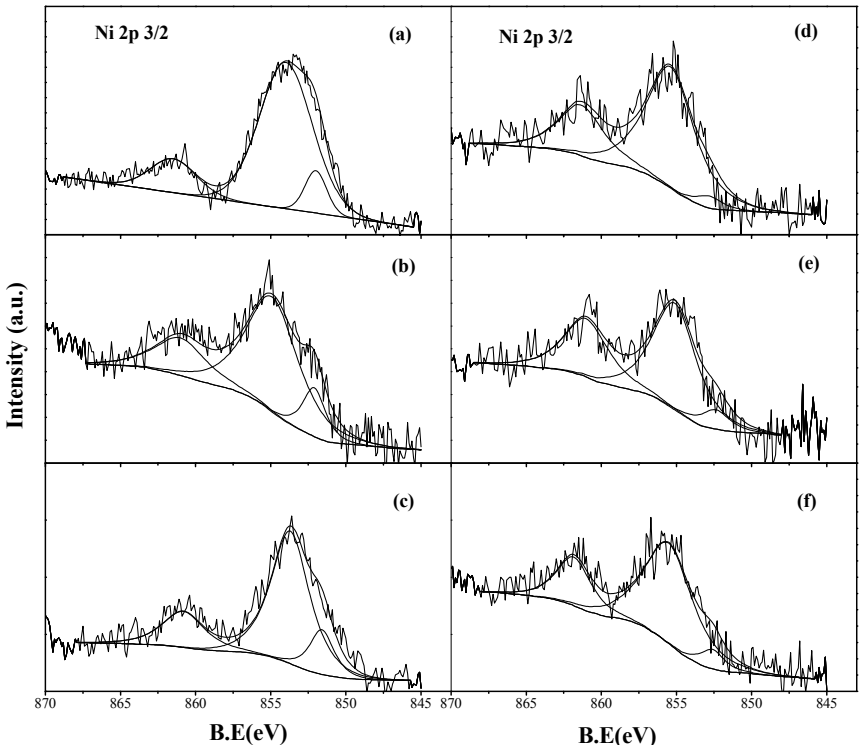


**Figure 5.** XPS of Ni $2p_{3/2}$ over the reduced catalysts (**a**) $MNC_{0.8}F_{0.0}$; (**b**) $MNC_{0.5}F_{0.3}$ and (**c**) $MNC_{0.0}F_{0.8}$; and spent catalysts of (**d**) $MNC_{0.8}F_{0.0}$; (**e**) $MNC_{0.5}F_{0.3}$; and (**f**) $MNC_{0.0}F_{0.8}$.

**Table 3.** The molar percentages of surface Ni/Fe species over the Ni-based catalysts from XPS.

| Species | $MNC_{0.8}F_{0.0}$ | | $MNC_{0.5}F_{0.3}$ | | $MNC_{0.0}F_{0.8}$ | |
|---|---|---|---|---|---|---|
| | Reduced | Spent | Reduced | Spent | Reduced | Spent |
| $Ni^0/(Ni^{0v}+Ni^{2+})$/% | 9.0 | 3.7 | 12.5 | 8.8 | 14.1 | 6.7 |
| $Fe^0/(Fe^0+Fe^{2+}+Fe^{3+})$/% | N.A. | N.A. | 70.9 | 12.9 | 77.6 | 4.6 |

For the Fe species in reduced catalysts, as shown in Figure 6, the spectra of Fe $2p_{3/2}$ can be deconvoluted into six peaks; among these peaks, the peak near 706.8 eV can be assigned to $Fe^0$, while other peaks near 709.8 eV, 710.8 eV, 711.6 eV, 712.6 eV, and 713.7 eV can be assigned to oxides of $Fe^{2+}/Fe^{3+}$ [22–24]. Over the reduced catalysts of $MNC_{0.5}F_{0.3}$ and $MNC_{0.0}F_{0.8}$ in Figure 6a,b and Table 3, there are strong peaks of $Fe^0$ with a molar ratio of $Fe^0/(Fe^0 + Fe^{2+} + Fe^{3+})$ near 70.9% and 77.6%, respectively, which is consistent with the strong peaks of Fe or Fe-rich Ni-Fe alloy in XRD (Figure 4a).

The reducible properties were also tested by temperature-programmed reduction (TPR). As shown in Figure 7, over the iron-free catalyst of $MNC_{0.8}F_{0.0}$ (Figure 7(1)), there are two weak reduction peaks: one weak peak starts from 343 °C to 650 °C and centers at 619 °C, which can be attributed to the reduction of surface or amorphous NiO species; the other high-temperature peak centered at 992 °C can be attributed to the reduction of nickel species in periclase of Mg(Ni)O [25], according to the result of XRD. These two weak reduction peaks suggest that only traces of Ni species were reduced below 650 °C, and is consistent with the result of XPS with only 9.0% of Ni species reduced.

With addition of iron in $MNC_{0.7}F_{0.1}$, one more reduction peak emerges near 836 °C, which can be mainly attributed to the phase of $Ca_2Fe_2O_5$, accordingly results of XRD (Figure 3b(2)). With more Fe and less Ca in $MNC_{0.5}F_{0.3}$ and $MNC_{0.3}F_{0.5}$, the phase of $Ca_2Fe_2O_5$ was weakened, as indicated by XRD (Figure 3b(3,4)), and the reduction peaks near 836 °C shrank; meanwhile, spinel phases ($MgFe_2O_4$, $NiFe_2O_4$ or $Fe_3O_4$) intensified, thus the reduction peaks near 600 °C and 890 °C intensified

accordingly. Over the Ca-free catalyst of $MNC_{0.0}F_{0.8}$, strong reduction peaks of Fe-containing spinel phases dominated the TPR profile, according to XRD file of Figure 3b(5).

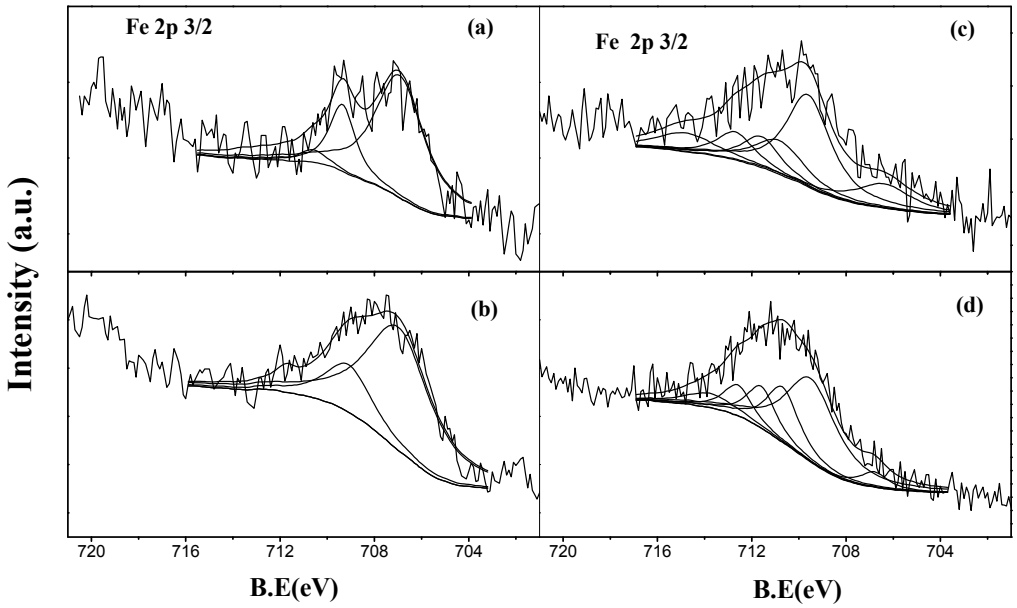


**Figure 6.** XPS of Fe $2p_{3/2}$ in the reduced catalysts of (**a**) $MNC_{0.5}F_{0.3}$ and (**b**) $MNC_{0.0}F_{0.8}$, and spent catalysts of (**c**) $MNC_{0.5}F_{0.3}$ and (**d**) $MNC_{0.0}F_{0.8}$.

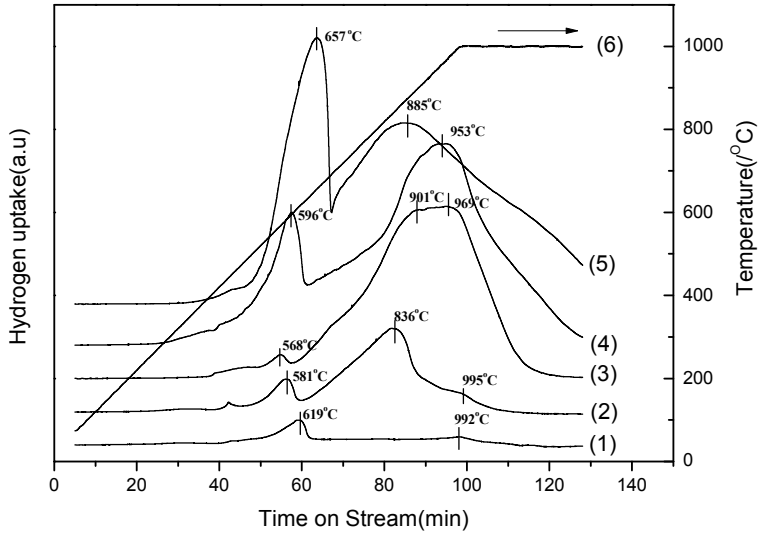


**Figure 7.** Profiles of temperature-programmed reduction of MNCF catalysts: (1) $MNC_{0.8}F_{0.0}$; (2) $MNC_{0.7}F_{0.1}$; (3) $MNC_{0.5}F_{0.3}$; (4) $MNC_{0.3}F_{0.5}$; and (5) $MNC_{0.0}F_{0.8}$; (6) temperature.

### 2.2.4. Spent Catalysts

To find the crystal variation after the ATR test, the spent catalysts were scanned by XRD. As shown in Figure 4b, the periclase phase still remained in the iron-free catalyst of $MNC_{0.8}F_{0.0}$, but the peaks of CaO shrunk remarkably with emergence of peaks of $CaCO_3$, suggesting that CaO was mainly transformed into $CaCO_3$ with $CO_2$ produced in the ATR process. With introduction of iron and decreasing content of Ca in $MNC_{0.7}F_{0.1}$, $MNC_{0.5}F_{0.3}$, and $MNC_{0.3}F_{0.5}$, the $CaCO_3$ and CaO phases were fading continuously and disappeared eventually; meanwhile, the peaks of periclase, which were weakening in the reduced catalysts, were intensifying in these spent catalysts. In the meantime, the

strong peaks of Fe or Ni-Fe alloy near 44.5° became weak, suggesting that the $Fe^0$ species could have been partly oxidized during ATR.

To verify the Fe and Ni species after ATR test, the spent catalysts were scanned by XPS. As shown in Figure 6c,d, after the ATR test, the peak of $Fe^0$ in $MNC_{0.5}Fe_{0.3}$ and $MNC_{0.0}F_{0.8}$ shrank remarkably with a molar ratio of $Fe^0/(Fe^0 + Fe^{2+} + Fe^{3+})$ near 12.9% and 4.6%, respectively, indicating that the Fe metal species did be oxidized and could form in the intensified phases of periclase as Mg(Ni,Fe)O, as shown in XRD of Figure 4b.

For the Ni species in the spent catalysts, as shown in Figure 5d,f, the peak of $Ni^0$ also became slightly weakened, and the ratio of $Ni^0/(Ni^0 + Ni^{2+})$ over the spent catalysts of $MNC_{0.8}F_{0.0}$, $MNC_{0.5}Fe_{0.3}$, and $MNC_{0.0}F_{0.8}$ were 3.7%, 8.8%, and 6.7%, respectively, suggesting that the additive of iron was helpful to resist the oxidation of $Ni^0$ during ATR.

Thermogravimetry (TG) was conducted as well, and minor weight loss (less than 1.8%) was recorded in these catalysts, while no carbon species were found in the spent catalysts in XRD of Figure 4b, suggesting that coking has been constrained in these Ni-based catalysts with basic support of MgO/CaO during ATR test.

## 3. Discussion

Based on the characterization results, one can find that the dolomite structure can be formed via hydrothermal synthesis with Pluronic P123. For the $MNC_{0.8}Fe_{0.0}$ catalyst without Fe ($MgNi_{0.2}Ca_{0.8}O_{2\pm\delta}$), dolomite was the main phase with trace of hydroxide of magnesium and nickel. After calcination, the dolomite precursors were transformed into periclase of solid solution as Mg(Ni)O and CaO. The $MNC_{0.8}Fe_{0.0}$ catalyst produced an AC conversion near 97.2% with a $H_2$ yield near 2.1 mol-$H_2$/mol-AC, because about 10.4% of AC was transformed into acetone.

With Ca partly replaced by Fe, dolomite still remained the main phase, while Fe-containing phases of hydrotalcite and spinel ($MgFe_2O_4$, $Fe_3O_4$, or $NiFe_2O_4$) were found in the precursor of $MNC_{0.5}Fe_{0.3}$ ($MgNi_{0.2}Ca_{0.5}Fe_{0.3}O_{2\pm\delta}$). After calcination, these phases were transformed into a main phase of periclase as Mg(Ni,Fe)O with high surface area and minor phases of $Ca_2Fe_2O_5$ and spinel. After reduction at 650 °C, main part of iron oxides (up to 70.9%) were reduced and formed in Fe-rich Ni-Fe alloy, or α-Fe metals, as shown in XRD (Figure 4a) and XPS (Figure 6). As a result, because of the synergetic effect of Fe and Ni with basic support of CaO-MgO in ATR [14,26], the AC in the feed completely converted, and the $H_2$ yield reached 2.6 mol-$H_2$/mol-AC and remained stable, while Ni species remained relatively stable with Fe promotion during ATR, as shown by XPS and XPD.

For $MNC_{0.0}Fe_{0.8}$ ($MgNi_{0.2}Fe_{0.8}O_{2\pm\delta}$) with Ca completely replaced by Fe, there were only Fe-containing spinel phases and weak magnesite phases formed; after calcination, the spinel phases with low surface area became the main phase. After reduction, strong peaks of α-Fe or Fe-rich Ni-Fe alloy were found from spinel phases; during the ATR test, although the conversion of AC was stable near 100%, the $H_2$ yield decreased to 2.1 mol-$H_2$/mol-AC, which can be attributed to part oxidization of $Fe^\circ$ as well as $Ni^0$ in Ni-Fe alloy, as shown in spent catalysts of XRD (Figure 4b) and XPS (Figures 5 and 6).

## 4. Materials and Methods

### *4.1. Catalyst Preparation*

Ni-based dolomite-derived catalysts were prepared via hydrothermal synthesis. Firstly, an aqueous solution of $Ni(NO_3)_2 \cdot 6H_2O$, $Ca(NO_3)_2 \cdot 4H_2O$, $Mg(NO_3)_2 \cdot 6H_2O$, and $Fe(NO_3)_3 \cdot 9H_2O$ was prepared, and precipitated by $Na_2CO_3$ with (total of metal cation electron charge)/($CO_3^{2-}$) = 4 at pH = 10.5 ± 0.5 under vigorous stirring, while NaOH was added as a pH adjuster. (The reagents mentioned in this sentence were purchased from Keshi Chemicals, Chengdu, Sichuan, China). After the precipitation process, a tri-block copolymer of (EO)20(PO)70(EO)20 (Pluronic P123, typical *Mn* = 5800, Sigma-Aldrich, St. Louis, MO, USA) with a molar ratio of Ni/P123 = 40 was added into the suspension.

The mixture was continuously stirred for 2 h at room temperature, transferred to an autoclave and remained at 150 °C for 36 h. The obtained precipitate was filtered and washed three times with distilled water, dried at 105 °C for 24 h, and calcined at 800 °C for 4 h in air. These Ni-based catalysts are listed in Table 1, while the weight compositions were checked by ICP-AES and are close to the nominal compositions.

### *4.2. Catalytic Performance Test*

ATR of acetic acid (AC) was conducted in a continuous-flow fixed-bed quartz-tubing reactor (I.D. 6 mm). 500 mg of catalyst (grain size of 20–40 mesh) was sandwiched between quartz wool in the reactor, and reduced in $H_2$ at 650 °C for 1 h before reaction. The mixture of water and AC (Keshi Chemicals, Chengdu, Sichuan, China) was then vaporized at 330 °C by a pre-heater, mixed with an $O_2/N_2$ gas,$N_2$ gas (Dongfeng Gas, Chengdu, Sichuan, China), and fed into the reactor with a molar ratio of $CH_3COOH:H_2O:O_2:N_2$ = 1:8:0.28:3.92 at 3.6 g-AC/(g-catalyst.h), 650 °C and 1 atm. The tail gas was analyzed online by a gas chromatography (GC-7890, Lunan Ruihong Instrument, Tengzhou, Shangdong, China) with TCD detectors via columns of carbon molecular sieves and Porapark Q (Sepulco Inc., Bellefonte, PA, USA), while $N_2$ was used as internal standard for analysis.

AC conversion ($X_{AC}$), selectivity of carbon-containing products ($S_i$), and hydrogen yield ($Y_{H2}$), were calculated according to the following equations:

$$X_{AC}(\%) = \frac{F_{AC\ in} - F_{AC\ out}}{F_{AC\ in}} \cdot 100$$

$$S_{i\ carbon-containing\ product}\ (\%) = \frac{F_{i\ carbon-containing\ product}}{ni(F_{AC\ in} - F_{AC\ out})} \cdot 100$$

$$Y_{H2} = \frac{F_{H2\ product}}{F_{AC\ in}}$$

In the above equations, $F_{i,\ in\ or\ out}$ is the molar flow rate of the $i$ species at the inlet or the outlet of the reactor, and $n_i$ is the stoichiometric factor between the carbon-containing products and acetic acid.

### *4.3. Catalyst Characterization*

The composition of catalysts was measured by elemental analysis with an inductively coupled plasma-atomic emission spectrometer (ICP-AES) (IRIS1000, Thermo Electron, Waltham, MA, USA).

The X-ray diffraction (XRD) patterns were recorded on an X-ray diffractometer (DX-2700, Haoyuan Instrument, Dandong, Liaoning, China) equipped with a graphite monochromator for Cu K$\alpha$ radiation.

Temperature-programmed reduction (TPR) was performed in a downstream fixed-bed quartz-tubing reactor at 10 °C/min in a flow of 5.0% $H_2/N_2$ by an adsorption instrument (TP-5076, Xianquan Instrument, Tianjin, China).

Specific surface areas and pore size of calcined samples were analyzed at −196 °C by $N_2$ physisorption on an automatic adsorption instrument (JW-BK112, JWGB, Beijing, China).

X-ray photoelectron spectroscopy (XPS) was recorded by a Kratos Axis-Ultra DLD spectrometer (Kratos Inc., Manchester, UK) using Al K$\alpha$ radiation (1486.6 eV). The binding energies were calibrated relative to the $C_{1s}$ peak from the carbon contamination at 284.6 eV.

Thermogravimetric analysis (TG) was conducted in air with a STA 409 PC/PG analyzer (NESZSCH, Selb, Germany) at a heating rate of 10 °C/min.

## 5. Conclusions

Dolomite-derived Ni-based catalysts with Fe additive, $MgNi_{0.2}Ca_{0.8-x}Fe_xO_{2\pm\delta}$ ($x$ = 0–0.8), were successfully synthesized via the hydrothermal synthesis method. From the dolomite precursors, phases of CaO and periclase-like solid solution of Mg(Ni,Fe)O with high surface area were formed with calcination. After reduction, there are more Ni species transformed into $Ni^0$ as Ni-Fe alloy, and these $Ni^0$ remained relatively stable during the oxidative atmosphere of ATR, as suggested by XRD and XPS, while the $Fe^0$ species were partly oxidized and formed in Mg(Ni,Fe)O. Meanwhile, because

of the basic support of CaO-MgO in the catalysts derived from the dolomite structure, coking has been constrained during the ATR test. As a result, the $MgNi_{0.2}Ca_{0.5}Fe_{0.3}O_{2\pm\delta}$ catalyst performed a stable reactivity in ATR: the conversion of AC reached 100%, and the $H_2$ yield remained stable around 2.6 mol-$H_2$/mol-AC.

**Acknowledgments:** This work was financially supported by National Natural Science Foundation of China (NSFC: 21276031), and International Cooperation program sponsored by Science & Technology Department of Sichuan Province of China (2015HH0013).

**Author Contributions:** The experimental work was designed by L.H. and X.Z.; X.Z, N.W., W.X., Y.D., and R.S. performed the experiments; X.Z., N.W. and L.H. analyzed the data; W.X. and N.W. contributed reagents/materials/analysis tools; X.Z., R.S. and L.H. drafted the paper. The manuscript was amended through the comments of all authors. All authors have given approval for the final version of the manuscript.

**Conflicts of Interest:** The authors declare no conflict of interest.

## References

1. Trane, R.; Dahl, S.; Skjøth-Rasmussen, M.S.; Jensen, A.D. Catalytic steam reforming of bio-oil. *Int. J. Hydrog. Energy* **2012**, *37*, 6447–6472. [CrossRef]
2. Ayalur Chattanathan, S.; Adhikari, S.; Abdoulmoumine, N. A review on current status of hydrogen production from bio-oil. *Renew. Sustain. Energy Rev.* **2012**, *16*, 2366–2372. [CrossRef]
3. Chen, T.; Wu, C.; Liu, R. Steam reforming of bio-oil from rice husks fast pyrolysis for hydrogen production. *Bioresour. Technol.* **2011**, *102*, 9236–9240. [CrossRef] [PubMed]
4. Li, Z.; Hu, X.; Zhang, L.; Liu, S.; Lu, G. Steam reforming of acetic acid over $Ni/ZrO_2$ catalysts: Effects of nickel loading and particle size on product distribution and coke formation. *Appl. Catal. A-Gen.* **2012**, *417–418*, 281–289. [CrossRef]
5. Mohanty, P.; Patel, M.; Pant, K.K. Hydrogen production from steam reforming of acetic acid over Cu–Zn supported calcium aluminate. *Bioresour. Technol.* **2012**, *123*, 558–565. [CrossRef] [PubMed]
6. Konsolakis, M.; Ioakimidis, Z.; Kraia, T.; Marnellos, G. Hydrogen Production by Ethanol Steam Reforming (ESR) over CeO2 Supported Transition Metal (Fe, Co, Ni, Cu) Catalysts: Insight into the Structure-Activity Relationship. *Catalysts* **2016**, *6*. [CrossRef]
7. Feng, M.S.; Liu, J.D.; Zhang, F.B.; Huang, L.H. Ni-based olivine-type catalysts and their application in hydrogen production via auto-thermal reforming of acetic acid. *Chem. Pap.* **2015**, *69*, 1166–1175. [CrossRef]
8. Seyedeyn Azad, F.; Abedi, J.; Salehi, E.; Harding, T. Production of hydrogen via steam reforming of bio-oil over Ni-based catalysts: Effect of support. *Chem. Eng. J.* **2012**, *180*, 145–150. [CrossRef]
9. Jang, W.-J.; Jeong, D.-W.; Shim, J.-O.; Kim, H.-M.; Han, W.-B.; Bae, J.W.; Roh, H.-S. Metal oxide (MgO, CaO, and La2O3) promoted Ni-Ce0.8Zr0.2O2 catalysts for H2 and CO production from two major greenhouse gases. *Renew. Energy* **2015**, *79*, 91–95. [CrossRef]
10. Nichele, V.; Signoretto, M.; Pinna, F.; Menegazzo, F.; Rossetti, I.; Cruciani, G.; Cerrato, G.; Di Michele, A. $Ni/ZrO_2$ catalysts in ethanol steam reforming: Inhibition of coke formation by CaO-doping. *Appl. Catal. B Environ.* **2014**, *150–151*, 12–20. [CrossRef]
11. Alipour, Z.; Rezaei, M.; Meshkani, F. Effects of support modifiers on the catalytic performance of $Ni/Al_2O_3$ catalyst in $CO_2$ reforming of methane. *Fuel* **2014**, *129*, 197–203. [CrossRef]
12. Huang, L.H.; Liu, Q.; Chen, R.R.; Hsu, A.T. Hydrogen production via auto-thermal reforming of bio-ethanol: The role of iron in layered double hydroxide-derived $Ni_{0.35}Mg_{2.65}AlO_{4.5+/\delta}$ catalysts. *Appl. Catal. A Gen.* **2011**, *393*, 302–308. [CrossRef]
13. Pighini, C.; Belin, T.; Mijoin, J.; Magnoux, P.; Costentin, G.; Lauron-Pernot, H. Microcalorimetric and thermodynamic studies of $CO_2$ and methanol adsorption on magnesium oxide. *Appl. Surf. Sci.* **2011**, *257*, 6952–6962. [CrossRef]
14. Djaidja, A.; Messaoudi, H.; Kaddeche, D.; Barama, A. Study of Ni–M/MgO and Ni–M–Mg/Al (M=Fe or Cu) catalysts in the $CH_4$–$CO_2$ and $CH_4$–$H_2O$ reforming. *Int. J. Hydrog. Energy* **2015**, *40*, 4989–4995. [CrossRef]
15. Hu, P.; Long, M. Cobalt-catalyzed sulfate radical-based advanced oxidation: A review on heterogeneous catalysts and applications. *Appl. Catal. B Environ.* **2016**, *181*, 103–117. [CrossRef]
16. Shang, R.; Duan, Y.; Zhong, X.; Xie, W.; Luo, Y.; Huang, L. Formic Acid Modified $Co_3O_4$-$CeO_2$ Catalysts for CO Oxidation. *Catalysts* **2016**, *6*. [CrossRef]

17. Mekhemer, G.A.H.; Halawy, S.A.; Mohamed, M.A.; Zaki, M.I. Ketonization of acetic acid vapour over polycrystalline magnesia: *in situ* Fourier transform infrared spectroscopy and kinetic studies. *J. Catal.* **2005**, *230*, 109–122. [CrossRef]
18. Guil-Lopez, R.; Navarro, R.M.; Ismail, A.A.; Al-Sayari, S.A.; Fierro, J.L.G. Influence of Ni environment on the reactivity of Ni–Mg–Al catalysts for the acetone steam reforming reaction. *Int. J. Hydrog. Energy* **2015**, *40*, 5289–5296. [CrossRef]
19. Zhang, F.B.; Wang, N.; Yang, L.; Li, M.; Huang, L.H. Ni-Co bimetallic MgO-based catalysts for hydrogen production via steam reforming of acetic acid from bio-oil. *Int. J. Hydrog. Energy* **2014**, *39*, 18688–18694. [CrossRef]
20. Adhlakha, N.; Yadav, K.L. Structural, dielectric, magnetic, and optical properties of $Ni_{0.75}Zn_{0.25}Fe_2O_4$-$BiFeO_3$ composites. *J. Mater. Sci.* **2014**, *49*, 4423–4438. [CrossRef]
21. Pintea, S.; Rednic, V.; Mărginean, P.; Aldea, N.; Tiandou, H.; Wu, Z.; Neumann, M.; Matei, F. Crystalline and electronic structure of Ni nanoclusters supported on $Al_2O_3$ and $Cr_2O_3$ investigated by XRD, XAS and XPS methods. *Superlattice Microst.* **2009**, *46*, 130–136. [CrossRef]
22. Biesinger, M.C.; Payne, B.P.; Grosvenor, A.P.; Lau, L.W.M.; Gerson, A.R.; Smart, R.S.C. Resolving surface chemical states in XPS analysis of first row transition metals, oxides and hydroxides: Cr, Mn, Fe, Co and Ni. *Appl. Surf. Sci.* **2011**, *257*, 2717–2730. [CrossRef]
23. Reddy, G.K.; Boolchand, P.; Smirniotis, P.G. Sulfur tolerant metal doped Fe/Ce catalysts for high temperature WGS reaction at low steam to CO ratios—XPS and Mössbauer spectroscopic study. *J. Catal.* **2011**, *282*, 258–269. [CrossRef]
24. Brajpuriya, R.; Shripathi, T. Investigation of Fe/Al interface as a function of annealing temperature using XPS. *Appl. Surf. Sci.* **2009**, *255*, 6149–6154. [CrossRef]
25. Lin, X.; Li, R.; Lu, M.; Chen, C.; Li, D.; Zhan, Y.; Jiang, L. Carbon dioxide reforming of methane over Ni catalysts prepared from Ni–Mg–Al layered double hydroxides: Influence of Ni loadings. *Fuel* **2015**, *162*, 271–280. [CrossRef]
26. Ren, J.; Qin, X.; Yang, J.-Z.; Qin, Z.-F.; Guo, H.-L.; Lin, J.-Y.; Li, Z. Methanation of carbon dioxide over Ni–M/$ZrO_2$ (M = Fe, Co, Cu) catalysts: Effect of addition of a second metal. *Fuel Process. Technol.* **2015**, *137*, 204–211. [CrossRef]